

# SPANWISE DIFFERENCES IN STATIC AND DYNAMIC STALL ON A PITCHING ROTOR BLADE TIP MODEL

C.B. Merz\*, C.C. Wolf†, K. Richter†, K. Kaufmann†, A. Mielke†, M. Raffel†

## Abstract

An experimental investigation of static and dynamic stall on a rotor blade tip model with a parabolic tip geometry and aspect ratio 6.2 at a chord Reynolds number of 900,000 and a Mach number of 0.16 is presented. The resulting flow is analyzed based on unsteady surface pressure measurements and quantitative flow visualizations by high-speed particle image velocimetry. The flow separation is found to be delayed near the parabolic blade tip for static angles of attack as well as for sinusoidal angle of attack motions. The maximum effective angle of attack prior to stall is shifted to approximately two-thirds of the span outboard from the root because of a positive twist of the model with an increasing geometric angle of attack towards the tip. The stall onset is observed near the section with the maximum effective angle of attack, with a subsequent spanwise spreading of the flow separation. Different stages of flow separation for static angles of attack are identified one of them with the occurrence of two stall cells. During dynamic stall, the leading edge vortex formation starts near the maximum effective angle of attack and the pitching moment peak resulting from the passage of the dynamic stall vortex is higher at this section. Further inboard the maximum aerodynamic loads are of comparable magnitude whereas the outboard section shows reduced peaks due to the influence of the wing tip vortex.

## NOMENCLATURE

$\alpha$	Angle of attack ( $^{\circ}$ )
$\dot{\alpha}$	Angular velocity ( $^{\circ}/s$ )
$\alpha_{\max}$	Maximum angle of attack at the wing root, for pitch oscillations
$\alpha_r$	Geometric angle of attack at the wing root ( $^{\circ}$ )
$\alpha_0$	Mean angle of attack at the wing root ( $^{\circ}$ )
$\alpha_1$	Amplitude of pitch oscillations ( $^{\circ}$ )
$c$	Airfoil chord (=0.27 m)
$C_d$	Sectional pressure drag coefficient
$C_l$	Sectional lift coefficient
$C_m$	Sectional pitching moment coefficient
$C_p$	Pressure coefficient
$f$	Frequency (Hz)
$k$	Reduced frequency: $k = \pi f c / U_{\infty}$
$M$	Mach number
$Re$	Reynolds number based on the model chord
$\rho_{\infty}$	Free stream flow density ( $kg/m^3$ )
$\sigma C_p$	Standard deviation of $C_p$
$U_{\infty}$	Free stream flow velocity (m/s)
$u, v, w$	Velocity components in $x, y$ and $z$ directions (m/s)

$x, y, z$	Local coordinates in chordwise direction, span and upward (m)
$x_{\text{sep}}$	Separation location (m)
$\uparrow$	during the upstroke of the pitching motion
$\downarrow$	during the downstroke of the pitching motion

## 1 INTRODUCTION

Dynamic stall is one of the major concerns in helicopter aerodynamics. The unsteady flow separation over parts of the rotor disk and the associated large excursions in the aerodynamic loads limit the flight envelope of modern helicopters. A fundamental understanding of the dynamic stall phenomenon is essential for improved modeling of the aerodynamics on a highly loaded main rotor. However, both measurements and computations in the rotor environment remain a challenging task and only few studies including dynamic stall have been carried out on full-scale rotors, e.g. [2, 7, 8, 9, 27]. Much of the knowledge on dynamic stall has been gained from experiments and computations on 2D airfoils. A review on dynamic stall on airfoils can be found in [15].

An extension of the 2D airfoil to include the influences of a tip vortex yet without rotation is a finite wing. By dynam-

\*Corresponding Author. German Aerospace Center (DLR), Institute of Aerodynamics and Flow Technology, Bunsenstr. 10, 37073 Göttingen, Germany, Christoph.Merz@dlr.de

†DLR-Institute of Aerodynamics and Flow Technology

ically changing the angle of attack beyond static stall, the influence of three-dimensionality on the dynamic flow separation and reattachment can be investigated. Two geometric options have been used in past studies: a cantilevered wing, e.g. [12, 14, 21, 24], and a wing with two free ends, e.g. [4].

The presence of a tip vortex was observed to delay the dynamic separation near the tip [24]. A leading edge vortex was found to form over a large portion of the span and then rapidly deform due to the faster convection of the dynamic stall vortex at the inboard sections and an “anchoring of the (dynamic stall) vortex to the tip” [13]. This inhibition of vortex convection was ascribed to the accumulation of spanwise vorticity at the blade tip [24]. The resulting vortex system is sometimes referred to as Omega-vortex because of its shape resembling the Greek capital letter  $\Omega$  in flow visualizations and Reynolds Averaged Navier-Stokes (RANS) computations, e.g. [11, 24, 25]. The tip vortex leads to a distortion of the pressure distribution at the tip of the wing resulting in a stronger negative pitching moment and increased lift within approximately 0.1 chord lengths inboard of the tip [12, 13]. Further inboard, a reduction in the maximum loads due to the suppressed dynamic stall vortex is observed while the flow near midspan is often described as similar to a 2D airfoil albeit with a reduced gradient of lift versus angle of attack.

Within the project *Stall and Transition on Elastic Rotor Blades (STELAR)* at the German Aerospace Center (DLR) a new wind tunnel model has been designed and wind tunnel experiments have been carried out to further improve the understanding of three-dimensional effects on dynamic stall and to establish an experimental data base for the validation of numerical codes. Emphasis is on the onset of stall and the subsequent spanwise spreading as well as on the role of the tip vortex in keeping the flow partially attached.

## 2 EXPERIMENTAL SETUP

In the current study the same experimental setup as detailed in [17] was used. The most important parameters are summarized in the following.

The wind tunnel model has a chord of 0.27 m and a span of 1.62 m. The blade tip is parabolic according to the specifications of the SPP8 blade tip without anhedral [20]. The DSA-9A airfoil with a maximum thickness-to-chord ratio of 9% is used along the entire span except for the innermost 0.1 m. Here, the airfoil thickness increases to a maximum of 18% of the chord with constant curvature transitions. This is necessary to transfer the bending moments caused by the aerodynamic forces to the shaft of the model. To minimize the influences of the wind tunnel walls and the wing root on the onset of stall the onset location should be on the outboard section near to the blade tip. This can be achieved with a positive twist of the wing, increasing the geometric angle of attack towards the blade tip. A positive linear twist from root to tip of  $5.5^\circ$  was applied here. As a result, the

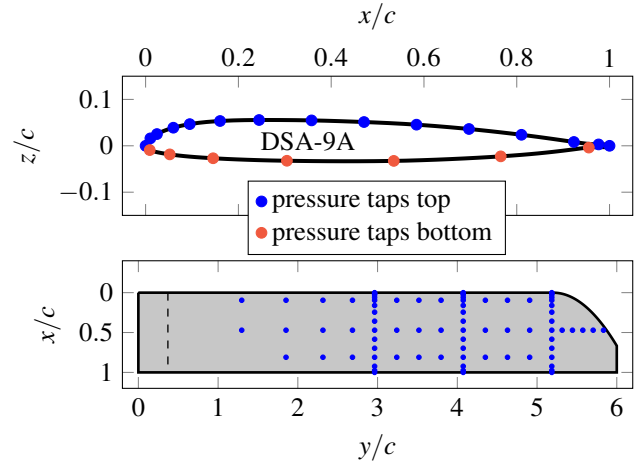


Figure 1: Airfoil and planform of the wind tunnel model indicating the locations of the pressure taps.

maximum effective angle of attack prior to stall is shifted away from the wing root. Using the numerical implementation of the lifting line method suggested in [1], the maximum effective angle of attack prior to static stall is at a distance of approximately 3.7 chord lengths from the root.

The model is equipped with 100 unsteady differential pressure transducers of type Kulite XCQ-093. Pressure taps are positioned in three sections with constant span around the airfoil and at three sections on the suction side with constant chordwise positions. The distribution of the pressure taps around the airfoil at the three sections at  $y/c = \{2.96, 4.07, 5.19\}$  can be seen on the top in fig. 1; an overview over the suction side is given at the bottom. Measured pressure distributions at these sections were integrated with a trapezoidal integration scheme to obtain the pressure part of the sectional lift, drag and pitching moment coefficients using the in-house tool *cp2cl* [5]. The transition from the increased airfoil thickness at the blade root to the regular DSA-9A airfoil is indicated by the dashed line at  $y/c = 0.37$ .

The experiments were carried out in the Side Wind Test Facility (SWG) at the German Aerospace Center in Göttingen. It is a closed-return wind tunnel with a maximum dynamic pressure of 2550 Pa corresponding to a free stream velocity of  $U_\infty \approx 65$  m/s. The test section is closed and has a width of 2.4 m and a height of 1.6 m. At the static stall angle, the blockage caused by the wind tunnel model is 3.7% of the wind tunnel cross section. The free stream velocity was set to  $U_\infty = 55$  m/s resulting in a Reynolds number based on the chord of 900,000 and a Mach number of 0.16.

The model was pitched around quarter-chord. An electric pitch actuation mechanism was used that is capable of sinusoidal motions of the angle of attack as well as ramps with constant angular velocity. The pitching motions are defined for the angle of attack at the blade root  $\alpha_r$  by the mean angle of attack  $\alpha_0$ , the amplitude  $\alpha_1$  and the frequency  $f$  as  $\alpha_r(t) = \alpha_0 + \alpha_1 \sin(2\pi ft - \pi/2)$ . Using the reduced fre-

quency  $k = \pi fc/U_\infty$ , the equation becomes

$$\alpha_r(t) = \alpha_0 + \alpha_1 \sin\left(\frac{2U_\infty}{c}kt - \frac{\pi}{2}\right). \quad (1)$$

In addition to the unsteady surface pressure measurements, the flow field above the suction side was measured in sections with constant span using stereoscopic particle image velocimetry (PIV). The flow was seeded with di-ethyl-hexyl sebacate (DEHS) droplets with a peak in the volumetric size distribution at  $0.8 \mu\text{m}$  using a PIVTEC PIV-part45 particle generator and a cyclone separator. A Litron LDY304 dual cavity laser and two PCO.dimax cameras were used for the illumination and image acquisition, respectively. The readout area of the camera chips was reduced to  $1680 \times 1472$  pixels to achieve a frame rate of 2 kHz. The cameras were operated in frame straddling mode resulting in an effective acquisition rate of 1 kHz for the PIV recordings. The particle images were processed with the Davis 8.1 software (LaVision) using a combined multigrid, multipass evaluation scheme. The final interrogation window size was  $16 \times 16$  pixels with an overlap of 50% resulting in a vector spacing of 1.81 mm or 0.67% of chord. The uncertainty of the velocity measurements depends on the precision of the time delay between the two images and the accuracy of the determined particle displacements. The time delay was verified to an accuracy of  $0.1 \mu\text{s}$  using a fast response photo diode. No variations in the time delay were found and therefore both random and bias errors due to a varying or an incorrect time delay are negligible. A discussion of the uncertainty in the particle displacements is presented in the following on the basis of sources of uncertainties discussed in [22]. The total error of the particle displacements can be decomposed as the sum of a random error and a bias error. Random samples of displacement histograms revealed no indication of peak locking, which constitutes the major part of the bias error. Therefore, the bias error is considerably smaller than 0.05 pixel and is neglected in the following. Two important contributions to the random error are small numbers of particle pairs and displacement gradients over each interrogation window. In flows with strong velocity gradients, for instance at the shear layer between the free stream and the separated flow behind a stalled airfoil, the displacement gradients over individual interrogation windows can be significant. In this case, reduced interrogation window sizes lead to smaller displacement uncertainties. At the same time, smaller interrogation windows reduce the number of particle image pairs. To maintain a sufficient number of particle image pairs, the in-plane and out-of-plane losses of particles have to be small. This can be achieved by adapting the time delay between two subsequent images and the seeding density. The parameters such as the time difference between the two PIV images, the seeding density, the intensity of the scattered light as well as the processing scheme were carefully adapted to the current setup. The exact algorithm of the multigrid, multipass processing within the Davis 8.1 software is not known to the authors. However, at least a

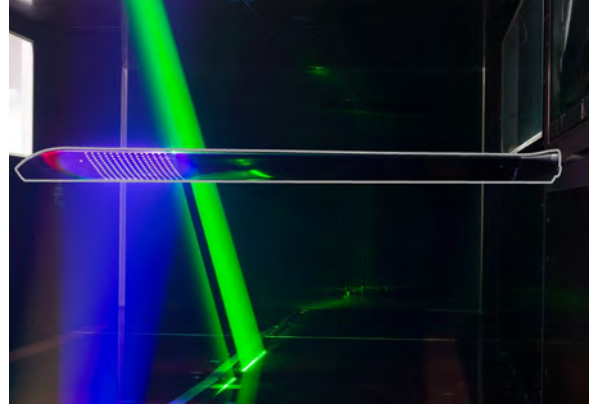


Figure 2: Wind tunnel model inside the test section viewed from upstream.

discrete window offset is expected. A random displacement error of 0.05 pixels or less [23] is therefore assumed. The resulting uncertainty in the velocity data is 1.8% of the free stream velocity  $U_\infty$ . Monte Carlo simulations in [22] have shown, that for particle shifts of less than half a pixel the random displacement error reduces approximately linearly. For the set of parameters used in this study, the uncertainty of the particle displacements is further reduced for velocities smaller than 10 m/s. A median test was applied to filter individual outliers. Where possible, the outliers were replaced by particle shifts based on secondary peaks in the cross-correlation and otherwise the missing data was interpolated. The amount of interpolated vectors is less than 0.5% of the total number of vectors.

The PIV acquisitions were synchronized to the pressure measurements which had a sampling rate of 20 kHz. The geometric angle of attack at the wing root  $\alpha_r$  was measured at the connection between the shaft of the model and the pitch actuation outside the test section. For this purpose two Micro-Epsilon optoNCDT LD-1605-20 laser-optical distance sensors were used which were sampled together with the pressure measurements. Figure 2 shows the wind tunnel model inside the test section viewed from upstream. The green laser light sheet is directed into the test section through a window on top whereas the cameras use the windows to the left and to the right of the test section downstream of the model. The illumination from the bottom and the markers on the pressure side of the model are used for optical deformation measurements.

### 3 RESULTS AND DISCUSSION

The flow around the finite wing is first characterized for static and quasi-static angles of attack. These results set the framework for the discussion of the dynamic stall on this rotor blade tip model. Subsequently, the influence of a sinusoidally varying angle of attack on the aerodynamics will be analyzed. Test cases including attached flow conditions,

and light and deep dynamic stall will be discussed.

### 3.1 Static Angle of Attack

An overview of the sectional aerodynamic coefficients at three spanwise locations as a function of the angle of attack at the wing root  $\alpha_r$  is given in fig. 3. The solid lines refer to data that was sampled during a quasi-steady  $\alpha_r$ -ramp with an angular velocity of  $\dot{\alpha} = 0.25^\circ/\text{s}$  up to  $\alpha_r = 15^\circ$  and was averaged over intervals of  $\Delta\alpha_r = 0.01^\circ$ . The filled symbols and the corresponding standard deviations pertain to measurements with static angles of attack between  $\alpha_r = 0^\circ$  and  $\alpha_r = 18^\circ$ . The aerodynamic coefficients reveal significant differences between the outboard section and the two sections further inboard. The lift slope at the outboard section is reduced while the pressure drag is higher than for the other two sections between  $\alpha_r = 0^\circ$  and  $\alpha_r = 11.1^\circ$ . Both effects can be explained by the proximity to the blade tip. The induced velocity of the tip vortex reduces the effective angle of attack and increases the pressure drag. Furthermore, distinct flow situations over the measured range of  $\alpha_r$  are visible in the aerodynamic coefficients. The most notable changes occur near  $\alpha_r = 11.1^\circ$  and  $\alpha_r = 14.7^\circ$ . Both

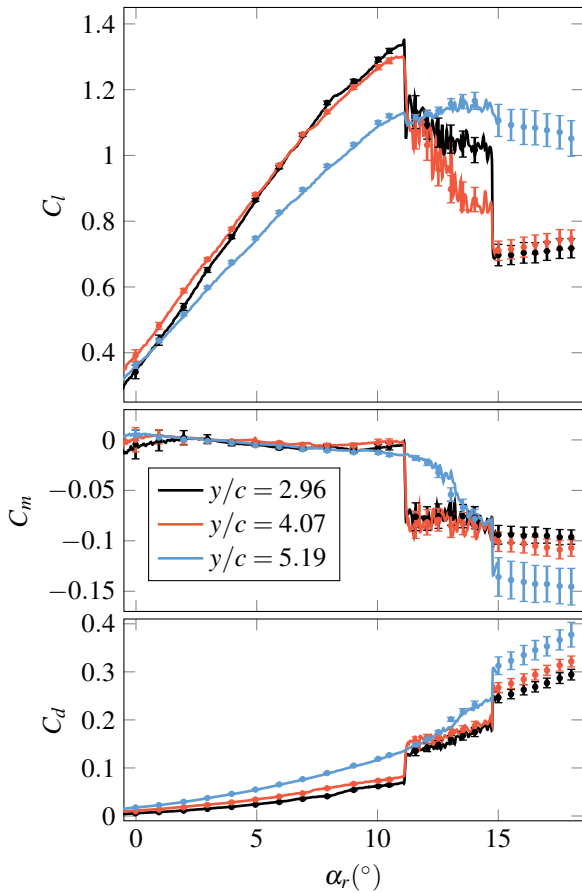


Figure 3: Sectional aerodynamic coefficients for a quasi-steady  $\alpha_r$ -ramp and static angles of attack at three spanwise sections.

are associated with sudden changes in the flow topology above the suction side corresponding to different stages of static stall, which will be elaborated in more detail in section 3.1.1. In between these two angles of attack, the lift coefficient at  $y/c = 4.07$  declines significantly more than at the other two sections. Also after the onset of static stall, there is a remarkable difference between the two sections at  $y/c = 2.96$  and  $y/c = 4.07$  compared with the section at  $y/c = 5.19$ . The stall onset at the outboard section is stretched over a much larger range of  $\alpha_r$ , similar to a trailing edge stall starting at  $\alpha_r = 11.1^\circ$  and not yet fully separated at the maximum angle of attack  $\alpha_r = 18^\circ$ . The sudden drop in lift and pitching moment at the two inboard sections at  $\alpha_r = 11.1^\circ$  is a classical hallmark of a leading edge type of stall. However, as will be discussed later, the flow does not separate from the leading edge until  $\alpha_r > 14.7^\circ$ . For  $\alpha_r > 14.7^\circ$ , all aerodynamic loads are higher at the most outboard location. The comparatively high lift coefficient is accompanied by a stronger negative pitching moment coefficient and a higher pressure drag.

There is also a more subtle influence of a flow separation on the suction side: At  $\alpha_r = 8.3^\circ$  there is a kink in the curve of the lift coefficient versus angle of attack for the section  $y/c = 2.96$ . At the same time, the pressure drag rises at that location. A likely cause for this effect is a separation near the trailing edge. A similar situation occurs for the section  $y/c = 4.07$  around  $\alpha_r = 7.2^\circ$ . In contrast, the outboard section does not show this effect.

#### 3.1.1 Different Stages of Static Stall

The aerodynamic coefficients depicted in fig. 3 reveal different stages of the static stall, the most dominant changes occur near  $\alpha_r = 11.1^\circ$  and  $\alpha_r = 14.7^\circ$ . Four representative flow situations at  $\alpha_r = \{10^\circ, 12^\circ, 14^\circ, 16^\circ\}$  will be discussed in detail in the following. Figure 4 shows the flow field as well as the pressure distribution, each at three sections with constant span. The pressure and velocity data is averaged over 100 samples. Due to limited optical access it was not possible to obtain flow field images at  $y/c = 2.96$ . Instead the measured flow fields at  $y/c = 2.78$  will be discussed together with the pressure distribution measured at  $y/c = 2.96$ .

At  $\alpha_r = 10^\circ$ , the flow is attached over most of the suction side of the wing. The flow separation near the trailing edge causing the kink in the  $C_l$  over  $\alpha_r$ -curve at the two inboard sections cannot be seen directly in the PIV recordings due to the insufficient spatial resolution. Nevertheless, a thicker wake at the two inboard sections compared to the outboard section is visible. The corresponding pressure distributions reveal a slightly negative pressure coefficient on the suction side near the trailing edge, indicating a local flow separation. The flow fields as well as the pressure distributions at the two inboard sections are qualitatively similar. The most notable difference occurs at the outboard location, where the suction peak is reduced to  $C_p \approx -4$  compared with  $C_p \approx -6$  at the inboard sections. This effect is

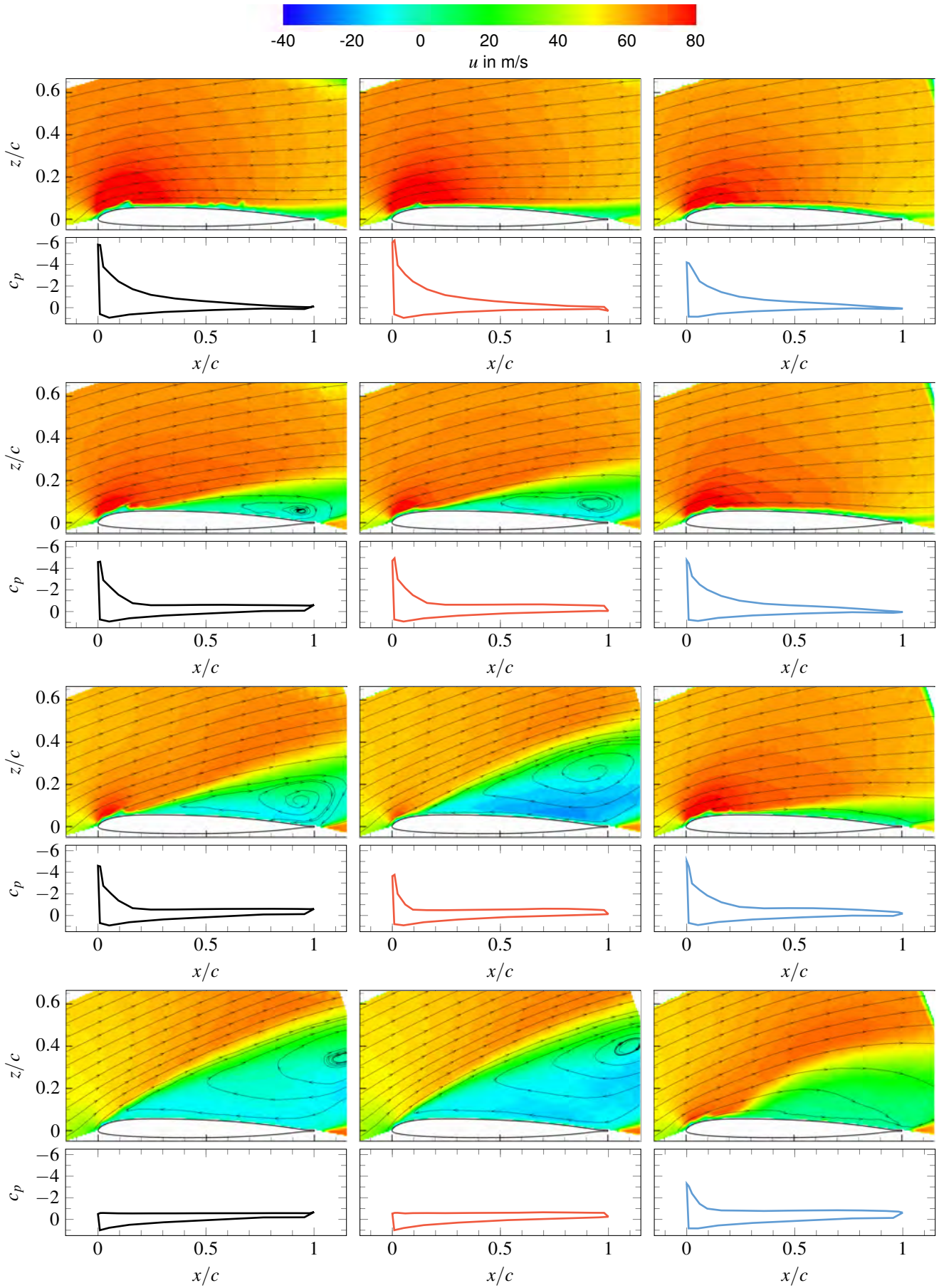


Figure 4: Averaged flow fields and pressure distributions for static angles of attack. Top to bottom:  $\alpha_r = \{10^\circ, 12^\circ, 14^\circ, 16^\circ\}$ . Left to right: flow fields at  $y/c = \{2.78, 4.07, 5.19\}$ , pressure distributions at  $y/c = \{2.96, 4.07, 5.19\}$ .

due to the induced downwash of the wing tip vortex.

The second row in fig. 4 at  $\alpha_r = 12^\circ$  corresponds to the situation after the onset of static stall at the two inboard sections. The suction peak is reduced to  $C_p \approx -4.9$  at  $y/c = 4.07$  and  $C_p \approx -4.6$  at  $y/c = 2.96$ . The pressure on the suction side between  $x/c = 0.24$  and  $x/c = 0.98$  is nearly constant around  $C_p = -0.6$  for both sections. The reduced suction near the leading edge results in a loss of lift and in combination with the decreased pressure near the trailing edge to a negative pitching moment and an increase in the pressure drag. The deviation of the stream lines and the pressure distributions indicates a flow separation that has moved forward to approximately 20% chord. This was also observed for an OA209 airfoil under static stall conditions [18]. At the section  $y/c = 5.19$  no influence of the static stall is evident. A flow field model for a low aspect ratio wing in static stall conditions has been derived in [26] based on surface oil flow visualizations. For the inboard sections, this flow field model predicts a laminar separation bubble near the leading edge, followed by a turbulent reattachment. A turbulent separation follows several percent of chord further downstream. Between the turbulent separation line and the trailing edge a recirculation zone is present. Near the tip of the rectangular wing the flow remains attached to the surface. All of these features correspond well with the observed flow on this blade tip model between  $y/c = 2.78$  and  $y/c = 5.19$ . Except for the laminar separation bubble and the boundary layer state these effects can be seen in fig.4. The spatial resolution of the current PIV setup is too small to observe a laminar separation bubble. For the airfoil shape and Reynolds number in this experiment, a laminar separation bubble near the leading edge at high angles of attack is likely. The method introduced in [6] to determine the boundary layer transition from surface pressure measurements was used for the quasi-static ramp motion. The transition location was found to lie between the pressure sensors at 1% and 2.5% chord for the three constant span sections prior the onset of static stall. This ascertains the assumption of a turbulent separation near  $x_{sep}/c \approx 0.2$ .

At  $\alpha_r = 14^\circ$ , corresponding to the third row in fig. 4, there is a notable difference between the flow field and pressure distributions between the two inboard sections. At  $y/c = 2.78$ , the height of the recirculation zone is slightly increased compared with  $\alpha_r = 12^\circ$ . The suction peak at  $y/c = 2.96$  is further reduced leading to a further reduction in lift. The change at  $y/c = 4.07$  is more drastic. The dividing stream line between the free stream and the recirculation zone moves significantly further away from the model surface. The suction peak is still present and can be detected as an area of increased velocity in the flow field near the leading edge as well as in the pressure distribution. The flow at  $y/c = 5.19$  is now also partly separated. The stream lines still follow the airfoil closely compared to the other sections. However, the extent of the wake in z-direction has increased from the previously discussed angle of attack.

With a further increase in the angle of attack, the flow separation eventually occurs at the leading edge. At

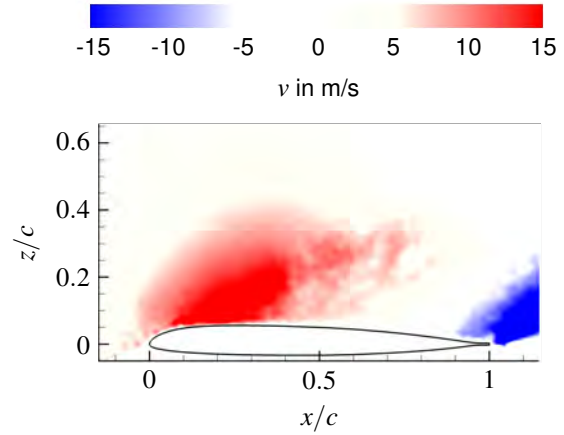


Figure 5: Averaged spanwise flow component at  $y/c = 5.19$  and  $\alpha_r = 16^\circ$ .

$\alpha_r = 16^\circ$ , the two inboard sections show a flow separation with a resulting recirculation zone extending over the entire suction side. The suction peaks have disappeared. Instead, the pressure coefficient on the suction side between 1% and 98% chord is nearly constant at  $C_p \approx -0.6$ . As a consequence, the lift has further dropped and the pressure drag is increased. There is also a large area of separated flow at  $y/c = 5.19$ . However, there is little to no recirculation within the  $x$ - $z$  plane due to the strong three-dimensionality of the flow near the parabolic blade tip. In fig. 5 the averaged velocity component in spanwise direction at the outboard section is shown, revealing a strong outboard motion near the leading edge and an inboard motion near the trailing edge. Due to the large separated area on the inboard section of the wing and the associated blockage effect, the flow is deviated towards the blade tip. This outboard component helps to maintain an attached flow in the first part of the suction side with a resulting suction peak at the leading edge. Between 16% and 98% chord there is a nearly constant pressure coefficient of  $C_p \approx -0.8$ . The remaining suction peak and the lower pressure over the rest of the chord compared with the other sections leads to the higher lift obtained at the outboard section.

The previous discussion has revealed significant differences in static stall at the three sections with constant span. A higher spanwise resolution is possible by analyzing the pressure data at constant chord. In fig. 6 the pressure coefficients at 9.5% chord for several spanwise positions and the four previously discussed angles of attack are given. The location between the suction peak and the turbulent boundary layer separation for  $11.1^\circ < \alpha_r < 14.7^\circ$  allows for a qualitative comparison of the suction peaks based on the measured pressures at 9.5% chord.

During mostly attached flow ( $\alpha_r = 10^\circ$ ), the pressure coefficients are comparatively homogeneous along the span. There is an increase in  $C_p$  towards the blade tip caused by the downwash induced by the wing tip vortex. A smaller

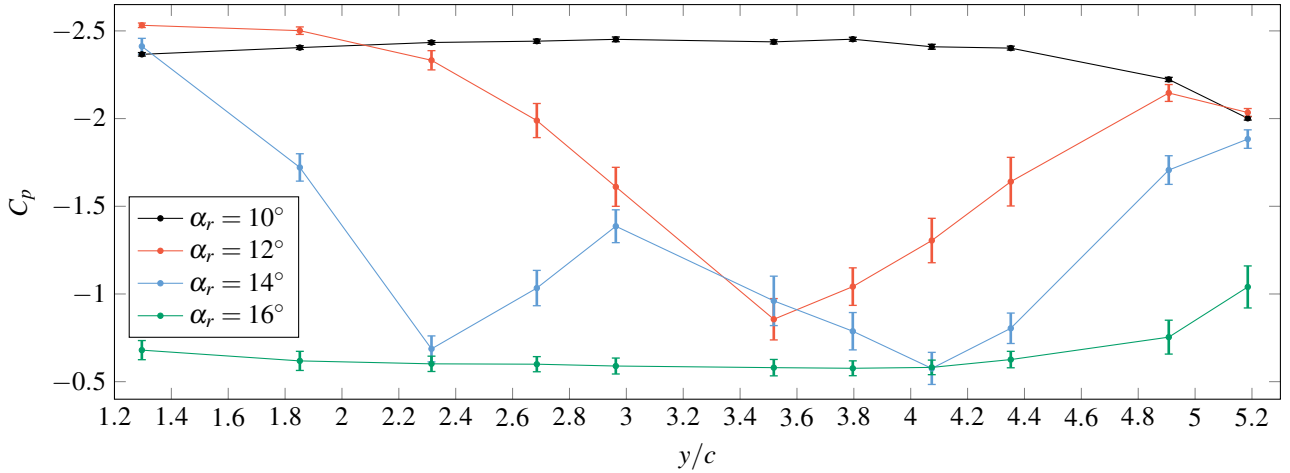


Figure 6: Pressure coefficients at 9.5% chord on the suction side at different stages of static stall.

increase in  $C_p$  is notable towards the blade root which is due to the reduced geometric angle of attack because of the positive twist of the model. The minimum value of  $C_p$  is reached at  $y/c = 3.80$ . The standard deviations around  $\sigma C_p = 0.01$  indicate steady flow conditions.

After the onset of static stall ( $\alpha_r = 12^\circ$ ), the suction between  $y/c = 2.31$  and  $y/c = 4.91$  is reduced with a maximum of  $C_p = -0.86 \pm 0.11$  at  $y/c = 3.52$ . The flow near the parabolic blade tip has been shown previously to be attached at this angle of attack. Furthermore, the flow for  $1.30 < y/c < 2.31$  appears to be mostly attached as well. The separation locations for the spanwise area with stalled flow are downstream of the pressure sensors at 9.5% chord. The higher pressure fluctuations expressed as increased standard deviations of  $0.10 < \sigma C_p < 0.14$  indicate an unsteady flow field upstream of the separation location which is likely to be caused by a chordwise motion of the separation location.

With a further increase in  $\alpha_r$ , the flow separation eventually spreads inboard. At  $\alpha_r = 14^\circ$  signs of a turbulent boundary layer separation are visible from  $y/c = 1.85$  to  $y/c = 4.91$ . At  $y/c = 5.19$  the suction is also slightly reduced. The reduced suction at 9.5% chord is not homogeneous along the span. There are two local maxima in  $C_p$  at  $y/c = 2.31$  and  $y/c = 4.07$ . The reduced suction indicates that the separation has moved furthest upstream at these two sections. At  $y/c = 2.96$  there is a local maximum in suction at 9.5% chord, resulting from a separation location further downstream compared with the neighboring sections. The spanwise variation in the separation location with two local maxima in the upstream separation location shows strong similarities to the observation of two stall cells for a wing with an aspect ratio of six [26].

At  $\alpha_r = 16^\circ$  the stall cells have disappeared. Instead, the flow is now separated from the leading edge over most of the span. While in the previous cases the sensor at 9.5% chord was upstream of the turbulent boundary layer separation, it is now downstream of the separation location for

most of the span. The outboard section now shows the strongest suction albeit also much reduced from the previous case. The standard deviations of  $C_p$  are smaller than for the previous cases where the separation location was downstream or near the sensor at 9.5% chord indicating a more steady flow situation although with higher fluctuations than the fully attached flow.

Regarding again the aerodynamic coefficients in fig. 3 and including the results of the previous paragraphs, several stages of flow separation on this rotor blade tip model are evident. First, a turbulent boundary layer separation occurs near the trailing edge of the inboard sections leading to an increase in pressure drag and a decrease in the gradient of the  $C_l$  over  $\alpha_r$ -curve. Around  $\alpha_r = 11.1^\circ$ , the turbulent separation moves rapidly forward to  $x/c \approx 0.2$ , leading to stalled flow over a large extent of the wing while the sections near the parabolic blade tip and towards the wing root show no signs of stall. With a further increase of  $\alpha_r$ , the stalled area increases inboard, leading to the formation of two stall cells. The stall now also becomes more evident on the outboard section. The remains of suction peaks near the leading edge indicate a turbulent boundary layer separation with varying separation locations  $x_{sep}/c$  over the span. While the increased pressure fluctuations indicate varying  $x_{sep}/c$  over time. For  $\alpha_r > 14.7^\circ$ , the flow is separated from the leading edge over most of the inboard sections leading to a complete breakdown of the suction peaks. Near the parabolic blade tip the turbulent boundary layer remains attached up to  $x_{sep}/c \approx 0.15$  resulting in a higher lift compared with the inboard sections.

The changes between these stages, especially at  $\alpha_r = 11.1^\circ$  and  $\alpha_r = 14.7^\circ$ , occur rapidly as indicated by the aerodynamic coefficients in fig. 3 while the stages itself appear stable over a range of angles of attack. In the following section, the transient behavior for the flow at  $\alpha_r > 11.1^\circ$  and the spanwise spreading of the stall will be discussed.

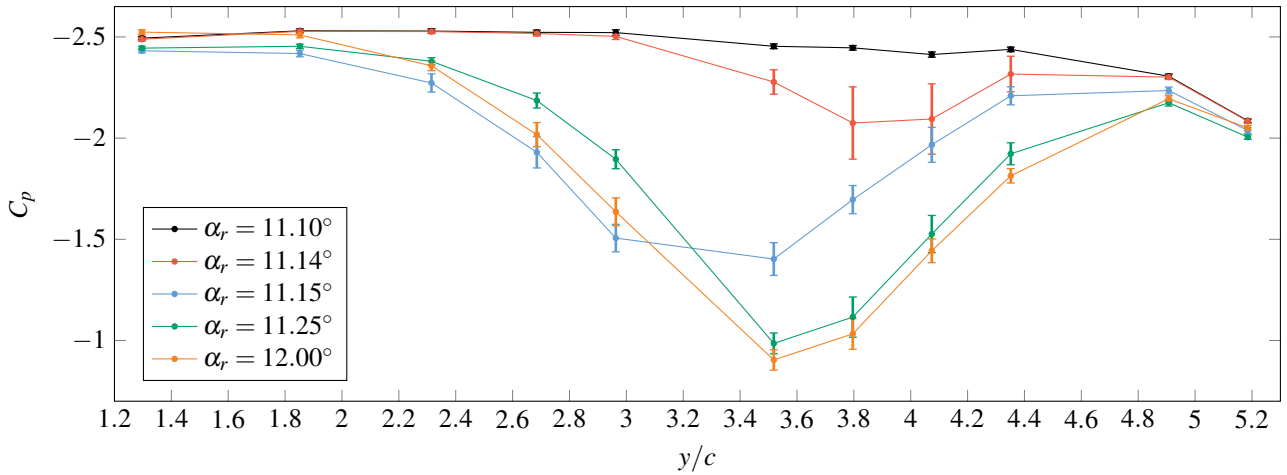


Figure 7: Pressure coefficients at 9.5% chord on the suction side at the onset of static stall.

### 3.1.2 The Transient Behavior of Static Stall

The previous results revealed an unsteady flow field after the occurrence of static stall with statistically steady mean values and elevated fluctuations in the pressure coefficients compared with the attached flow. Another interesting aspect is the temporal evolution at the onset of static stall with the associated spanwise spreading of the flow separation. Because this transient phenomenon cannot be captured with a static angle of attack, data from the  $\alpha_r$ -ramp with  $\dot{\alpha} = 0.25^\circ/\text{s}$  has been used.

In fig. 7 the spanwise pressure coefficients at 9.5% chord are shown. At  $\alpha_r = 11.14^\circ$  the first decrease in suction occurs between  $y/c = 3.52$  and  $y/c = 4.35$ . The  $C_p$ -values inboard of  $y/c = 2.96$  and outboard of  $y/c = 4.91$  are comparable to the pre-stall values at  $\alpha_r = 11.10^\circ$ . Within  $\Delta\alpha_r = 0.01^\circ$  corresponding to a time difference of 0.04 s, the stalled area spreads further inboard to  $y/c = 2.31$  accompanied by a further decrease in suction at 9.5% chord. At  $\alpha_r = 11.25^\circ$ , the spanwise extent of the reduced suction has reached a nearly stable condition. The maximum reduction in suction occurs at  $y/c = 3.52$  with a resulting  $C_p = -0.99 \pm 0.05$ . With increasing angle of attack, the suction in the stalled areas reduces further, whereas for the unstalled sections a slight increase is measurable.

The initiation of static stall is shown to occur over a limited spanwise area around two chord lengths inboard of the wing tip and then to propagate rapidly inboard. The stall onset is a consequence of the maximum effective angle of attack prior to static stall in this area as discussed in chapter 2.

## 3.2 Dynamic Angle of Attack

In the following sections, the dynamic stall on the pitching rotor blade tip model is discussed. The analysis begins with cases ranging from attached flow throughout the pitching cycle to light dynamic stall. Furthermore, test cases with deep dynamic stall will be presented. As for the static case,

spanwise differences in the onset and propagation of stall will be highlighted.

### 3.2.1 Attached Flow to Light Dynamic Stall

In section 3.1.2 it was shown that the static stall starts near  $y/c = 4$ . For the dynamic stall, the onset is expected to be located near the static stall onset. In fig. 8 the phase averaged sectional aerodynamic coefficients at  $y/c = 4.07$  are shown for four different mean angles of attack  $\alpha_0 = \{5.0^\circ, 5.5^\circ, 6.0^\circ, 6.5^\circ\}$  with an amplitude of  $\alpha_1 = 6^\circ$  and a reduced frequency of  $k = 0.05$ . For  $\alpha_0 = 5^\circ$  the static stall angle is never exceeded during the pitching motion. Therefore no excursions of the aerodynamic loads due to stall are expected. The lift coefficient shows a small reduction on the downstroke shortly after the upper turning point  $\alpha_{\text{max}}$  of the angle of attack motion. This can be attributed to the previously discussed flow separation near the trailing edge. On the lower branch ( $\alpha_r < 7^\circ$ ) there is a small hysteresis in the lift coefficient with the higher lift during the downstroke as a result of the pitching motion. Pitching moment as well as pressure drag also show hystereses but no significant excursions outside the range for the unstalled static wing. Increasing the mean angle of attack to  $\alpha_0 = 5.5^\circ$ , the static stall angle is now exceeded at  $\alpha_{\text{max}}$ . Nevertheless, there is only a mild reduction in lift near the upper turning point and no indication of stall in the pitching moment and pressure drag. In [16] this condition was stated as “a measure of the maximum useful lift that a given airfoil can deliver if drag rise and moment stall are to be avoided.” This definition can be extended for the finite wing as the maximum lift attainable without negative influences on the aerodynamic loads for the given set of flow and motion parameters. With a further increase of  $\alpha_0$ , the occurrence of dynamic stall is visible in the loops of the pitching moment and pressure drag coefficients. One major concern for the dynamic stall on a helicopter rotor blade is the sharp peak in the nose-down pitching moment. For  $\alpha_0 = 6^\circ$ , the minimum

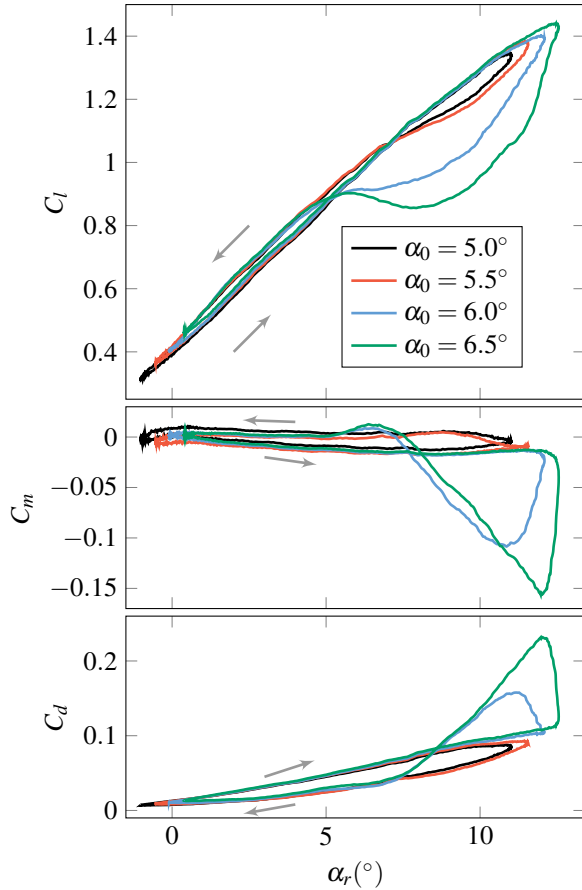


Figure 8: Phase averaged sectional aerodynamic coefficients at  $y/c = 4.07$  for different mean angles of attack with  $\alpha_1 = 6^\circ$  and  $k = 0.05$ .

of the phase averaged pitching moment coefficient already exceeds the pitching moment for the statically stalled wing up to  $\alpha_r = 14.7^\circ$ . Increasing the mean angle of attack further, there is only a minor gain in the maximum lift, however, at the cost of an even stronger negative pitching moment.

An important parameter for the performance of an airfoil is the maximum lift  $C_{l,max}$ . For dynamic stall conditions another important parameter is the negative pitching moment peak  $C_{m,min}$ . To compare the characteristics of the different spanwise sections, these two parameters can be evaluated for both static and dynamic conditions. Figure 9 depicts the minimum  $C_m$  versus the maximum  $C_l$  for different static and dynamic cases. Note that the values for  $C_{l,max}$  and  $C_{m,min}$  for the dynamic cases differ between fig. 8 and fig. 9 because the former is based on phase averaging of 160 cycles while the latter is based on conditional averaging of the extremal values for the same 160 cycles. The color indicates the spanwise section of the data and the symbol corresponds to the test case. Standard deviations in both  $C_{l,max}$  and  $C_{m,min}$  are indicated for all sections when stall occurs at any one of the sections.

In section 3.1 it was shown that the static stall angle is at  $\alpha_r = 11.1^\circ$  and the stall onset is characterized by a sig-

nificant drop in lift at the two inboard sections. The static  $C_{l,max}$  is therefore obtained just before the stall onset and the values for all three sections are indicated by asterisks in fig. 9. The situation after the onset of static stall, measured at a static  $\alpha_r = 11.5^\circ$ , is represented by triangles. The lift has dropped at the two inboard sections, there is a nose-down pitching moment and both lift and pitching moment exhibit strong fluctuations. On the contrary, lift and pitching moment show only minor changes at the outboard sections with smaller fluctuations. Comparing the static performance with the dynamic cases, an increase in the lift coefficient at all sections is evident. Revisiting the concept of maximum useful lift, the test case with  $\alpha_0 = 5.5^\circ$  appears as the limiting case. The maximum lift coefficient at  $y/c = 4.07$  is  $C_{l,max} = 1.41 \pm 0.01$  which is about  $\Delta C_{l,max} = 0.12$  higher than the maximum lift at this section for a static angle of attack. The strongest negative pitching moment at all sections shows only standard deviations and is less than the pitching moment after the onset of static stall for the two inboard sections. A slight increase in  $C_{l,max}$  leads to a strong increase in the negative pitching moment at  $y/c = 4.07$ . In contrast, the other two sections show little to no effects of dynamic stall. For  $\alpha_r \leq 12^\circ$ , the outboard section has shown no signs of stall for static angles of attack. For dynamic motions with a maximum angle of attack  $\alpha_{max} \leq 12^\circ$ , there appears also no significant negative pitching moment. The small standard deviations indicate a high repeatability over all cycles. With  $\alpha_0 = 6.5^\circ$ ,  $C_{m,min}$  reduces slightly but with a significant standard deviation, resulting from an increased nose-down pitching moment for some of the cycles. The situation at  $y/c = 2.96$  shows some unique characteristics as well. For a static  $\alpha_r = 11.5^\circ$ , the turbulent boundary layer separation has reached a position in the first quarter of the chord, similar to the section  $y/c = 4.07$  but different from  $y/c = 5.19$ . For the dynamic cases with  $\alpha_{max} \leq 12^\circ$  there

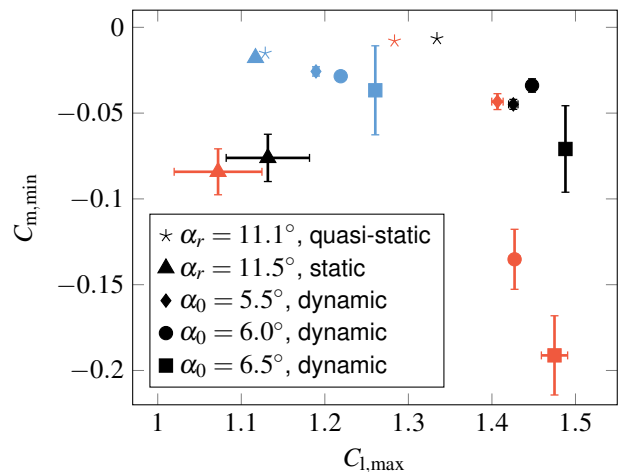


Figure 9: Conditionally averaged maximum lift and negative pitching moment peak at  $y/c = 2.96$  (black),  $y/c = 4.07$  (red) and  $y/c = 5.19$  (blue). All dynamic cases have an amplitude  $\alpha_1 = 6^\circ$  and a reduced frequency  $k = 0.05$ .

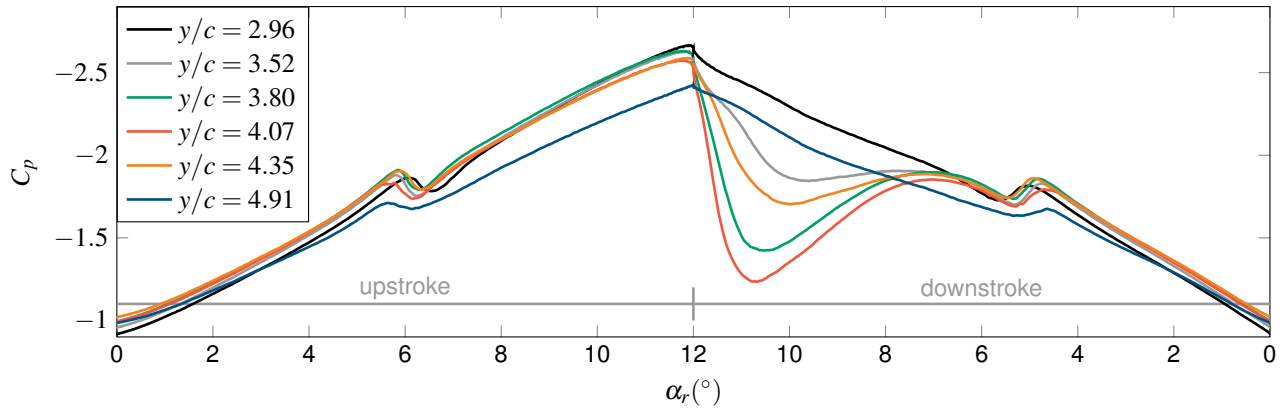


Figure 10: Phase averaged pressure coefficients at 9.5% chord on the suction side for  $\alpha_0 = 6^\circ$ ,  $\alpha_1 = 6^\circ$  and  $k = 0.05$ .

is very little influence of a flow separation detectable. The maximum lift increases while the minimum pitching moment remains close to the static values. At  $\alpha_0 = 6.5^\circ$  the pitching moment peak increases with higher fluctuations similar to the section at  $y/c = 5.19$ .

The previous discussion has revealed that the light dynamic stall on the pitching rotor blade tip model is limited to a spanwise area around  $y/c = 4.07$ . Increasing the maximum angle of attack of the pitching motion while maintaining both amplitude and reduced frequency leads to a further increased nose-down pitching moment at  $y/c = 4.07$  and a spreading in spanwise direction of the effects of dynamic stall, namely the increased fluctuations in  $C_{m,\min}$ . To examine the spanwise extent of light dynamic stall, the phase averaged pressure coefficients at 9.5% chord are plotted over the angle of attack for several sections in fig. 10. The pressure coefficients indicate a reduced suction between  $\alpha_r = 12^\circ$  and  $\alpha_r = 7^\circ$  if the separation point of the turbulent boundary layer moves upstream. For the shown pitching motion of  $\alpha_0 = 6^\circ$ ,  $\alpha_1 = 6^\circ$  and  $k = 0.05$ , the stalled area includes the sections between  $y/c = 3.52$  and  $y/c = 4.35$  with the strongest increase in  $C_p$  at  $y/c = 4.07$ . At  $y/c = 4.91$  the influence of the induced downwash of the tip vortex manifests itself in a reduced suction over most of the pitching cycle.

Note the distortions in the pressure coefficient distributions around  $\alpha_r = 6^\circ$  on the upstroke and after  $\alpha_r = 5.2^\circ$  on the downstroke. These are associated with the movement of the boundary layer transition over the 9.5% chord position, indicating a turbulent boundary layer upstream of 9.5% chord for all sections when stall occurs.

### 3.2.2 Deep Dynamic Stall

Figure 11 depicts the phase averaged sectional aerodynamic coefficients for a pitching motion of  $\alpha_0 = 9^\circ$ ,  $\alpha_1 = 6^\circ$  and  $k = 0.05$ . The large excursions of all aerodynamic coefficients indicate deep dynamic stall conditions for the two inboard sections. Similar to the measurements with static angles of attack, the lift at the two inboard sections is of com-

parable magnitude and shows a stronger increase with increasing angle of attack for attached flow than the outboard section. A lift overshoot occurs almost simultaneously at the two inboard sections with a peak at  $\alpha_r = 14.5^\circ$ . Subsequently, the lift coefficient drops at both sections. There is a second increase in lift at  $y/c = 2.96$  which culminates in a second peak in  $C_l$  at the turning point of the motion. At the same time, the maximum lift at the most outboard section is reached, while at  $y/c = 4.07$  the lift has already started to decrease rapidly. For a large part of the downstroke, during massively stalled flow conditions the highest lift is generated at the outboard section.

The course of the pitching moment shows the occurrence of sudden sharp peaks. The moment stall, defined as the start of the deviation from unstalled values, occurs first at section  $y/c = 4.07$ , followed by  $y/c = 2.96$  and then  $y/c = 5.19$ . The negative peak in the pitching moment is smaller for the outboard section. However, for the largest part of the downstroke, the pitching moment at that section is stronger than at the other two sections.

The pressure drag is highest for the outboard section for most of the pitching cycle due to the influence of the tip vortex. Only the peak in pressure drag associated with the passage of the dynamic stall vortex is higher at the two inboard sections.

Comparing the general trend of the sectional aerodynamic coefficients for the dynamic stall test case with the static stall, similarities can be observed. For attached flow, the lift at the outboard location is considerably less than at the two inboard sections. This trend reverses when significant flow separation is present on the wing. The higher lift is a result of a remaining suction peak near the leading edge when the flow has separated from the leading edge at the inboard sections. The flow near the leading edge in the proximity to the parabolic blade tip has a strong component towards the blade tip for both static and dynamic stall. This has been shown in fig. 5 for static stall and in [17] for dynamic stall using tuft visualization on the rotor blade tip model used in this work. Similarly, the negative pitching moment and pressure drag are stronger at the outboard

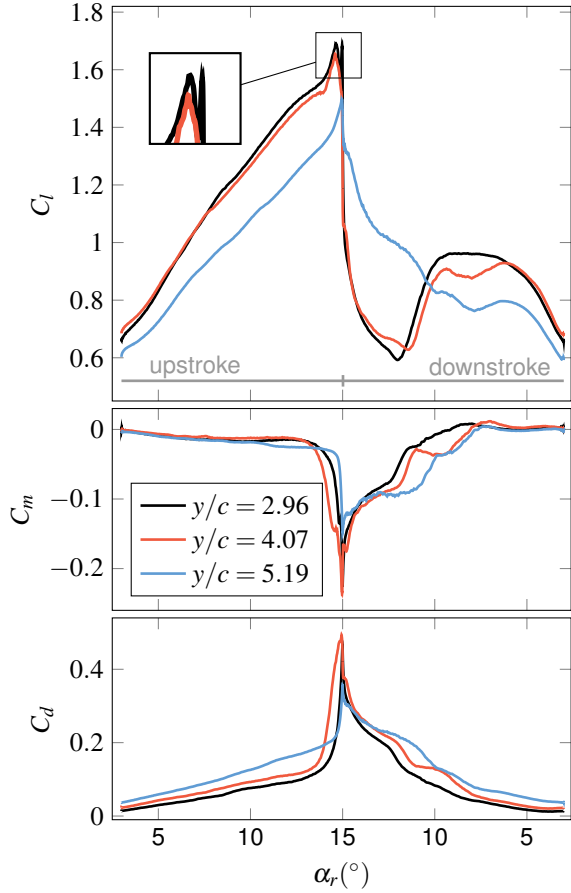


Figure 11: Phase averaged sectional aerodynamic coefficients for a motion of  $\alpha_0 = 9^\circ$ ,  $\alpha_1 = 6^\circ$  and  $k = 0.05$ .

section in the post stall phase compared to the inboard sections. One major difference between static stall and dynamic stall in general is the occurrence of sharp peaks in the aerodynamic coefficients. These peaks are associated with the formation and convection of a large coherent structure often referred to as the dynamic stall vortex. For the finite wing used in this study, the peaks are stronger at the inboard sections with the maximum lift for this case reached at  $y/c = 2.96$  and the strongest negative pitching moment as well as highest pressure drag at  $y/c = 4.07$ . The hindered convection of the dynamic stall vortex due to the streamwise vorticity generated near the blade tip results in a smaller lift overshoot and reduced peaks in the negative pitching moment and pressure drag at the outboard section.

Figure 12 shows the instantaneous flow fields and pressure distributions at three sections for  $\alpha_r = 14.5^\circ$ . This corresponds to the first peak in lift at the inboard sections. Note that the most inboard flow field is measured at  $y/c = 2.78$  due to limited optical access at the most inboard pressure distribution ( $y/c = 2.96$ ). Despite the comparable lift values inboard, the underlying flow structures are different. The inboard section displays an increased suction peak of  $C_p = -10$  at the leading edge with an ensuing positive pres-

sure gradient. The flow is attached around the leading edge to about 20% chord. The height of the shear layer between the recirculation zone and the free stream is comparable to the airfoil thickness. At  $y/c = 4.07$  the flow separation has progressed further upstream and there is a reduced suction peak at the leading edge. A strong reverse flow above the suction side around 10% chord is visible (see also close-up in fig. 13). Together with the accelerated flow around the leading edge this leads to a local swirling motion and the associated pressure distribution has a local minimum at 9.5% chord. The distance of the separated shear layer from the model surface is larger compared with the inboard section. The different flow topologies can be interpreted as different stages of dynamic stall as defined for a pitching airfoil. According to the definition in [3] the inboard section shows a flow reversal over much of the airfoil chord while at  $y/c = 4.07$  a leading edge vortex is already forming. Using the notation of [19], the inboard section is in the primary instability stage while the flow at  $y/c = 4.07$  corresponds to the vortex formation stage.

The outboard section displays no sign of stall at this angle of attack. There is an increased suction peak at the leading edge compared to static angles of attack and a slightly negative pressure coefficient near the trailing edge indicating a small flow separation in this area.

For the model used in the current study, a flow reversal occurs on the suction side and progressively moves upstream prior to the development of a dynamic stall vortex, similar to the observations in [3] for a pitching airfoil. As a consequence, there is an upstream movement of the separation location. The reattachment occurs from the leading edge towards the trailing edge, with a resulting downstream motion of the separation point. For the estimation of the separation locations, a criterion similar to the one derived in [18] has been developed. Flow separation was detected at the most upstream location where the velocity tangential to the airfoil at a wall-normal distance of 3 mm was smaller than the  $l^2$ -norm of the other two velocity components. For increased robustness, this criterion had to be true for six subsequent PIV data points. The results are shown in fig. 14 by the phase averaged separation points at three sections plotted versus  $\alpha_r$ . The flow fields on which this evaluation is based have been recorded for ten successive pitching cycles and during parts of the cycle with separated flow for each section. The standard deviations are calculated based on a truncated normal distribution bounded from zero to one [10]. The first upstream motion of the separation location occurs at section  $y/c = 4.07$ . After exceeding the static stall angle  $\alpha_r = 11.1^\circ$ , the separation is detected near the trailing edge and moves upstream to about  $x/c = 0.8$  until  $\alpha_r = 13^\circ$ . Then, a rapid movement of the separation location to the most upstream point ensues. Due to the positioning of the cameras downstream of the model, the leading edge is not visible in the PIV recordings and the most upstream separation point in the PIV data is at 5% chord. The corresponding pressure distribution shows a separation from the leading edge. The standard devia-

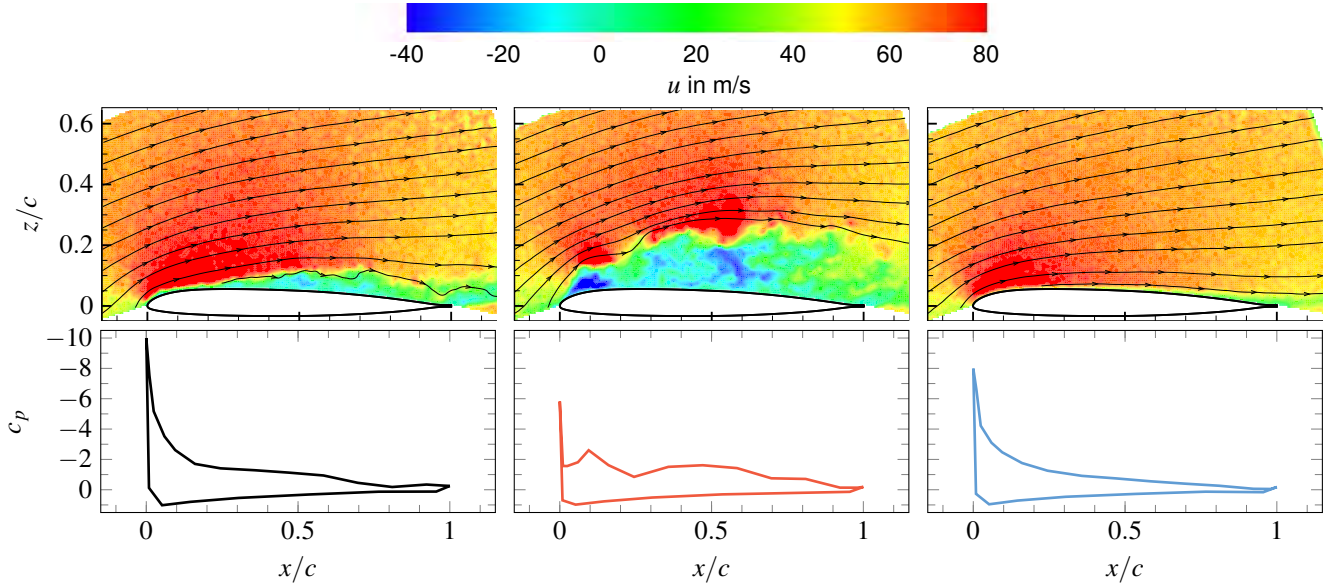


Figure 12: Instantaneous flow fields and pressure distributions at  $\alpha_r = 14.5^\circ \uparrow$  during a pitching motion of  $\alpha_0 = 9^\circ$ ,  $\alpha_1 = 6^\circ$  and  $k = 0.05$ . Left to right: flow fields at  $y/c = \{2.78, 4.07, 5.19\}$ , pressure distributions at  $y/c = \{2.96, 4.07, 5.19\}$ .

tions during the upstream motion of the separation point is small, indicating only minor variations between individual cycles at this section. The separation location at section  $y/c = 3.15$  moves upstream at higher angles of attack compared with  $y/c = 4.07$ . Nevertheless, the upstream motion up to the leading edge occurs entirely during the upstroke. At the outboard section no separation is detected until  $\alpha_{\max}$  is reached. Similar to the static stall, an area of attached flow around the leading edge remains over the entire pitching cycle. The standard deviations show strong variations in the separation location at  $y/c = 5.19$  between the individual cycles with mean values around  $x/c = 0.6$  for most of the times when flow separation is present. The sequence of the dynamic reattachment along the span differs from the dynamic separation. The start of the dynamic reattachment is at  $y/c = 3.15$ , reaching fully attached flow conditions at  $\alpha_r = 8^\circ \downarrow$ . The standard deviations during reattachment are higher than during dynamic separation due to larger differences between the individual cycles of the reattachment initiation and propagation. Although the flow separation near the parabolic blade tip occurred much delayed compared to the inboard sections, the reattachment happens nearly at the same time as at section  $y/c = 4.07$ .

The previously discussed results revealed the onset of static as well as dynamic stall near  $y/c = 4$ . The flow separation first moves upstream in this area. After stall initiation, a spanwise spreading has been observed. Depending on the severity of the dynamic stall, only parts of the finite wing model can be affected. For deep dynamic stall, the vortex formation is also initiated near  $y/c = 4$ . Keeping the geometric parameters of the pitching motion (mean angle of attack and amplitude) fixed, the influence of the unsteadiness on the spanwise spreading can be investigated. A comparison of the maximum sectional aerodynamic loads

for different reduced frequencies with  $\alpha_0 = 9^\circ$  and  $\alpha_1 = 6^\circ$  is given in fig. 15. Note the different scaling compared to fig. 9. All aerodynamic loads are well beyond the values for static stall. At the smallest reduced frequency of  $k = 0.025$  the differences in both  $C_{l,\max}$  and  $C_{m,\min}$  are small between the three sections. Overall, at section  $y/c = 2.96$  the highest lift is obtained while the strongest negative pitching moment occurs at  $y/c = 4.07$ . Increasing the reduced frequency to  $k = 0.05$ , a wider spread in the maximum loads becomes evident. This case corresponds to the previously discussed deep dynamic stall case. As for the phase averaged aerodynamic loads in fig. 11, the conditionally averaged lift and moment coefficients are similar between the two inboard sections but significantly reduced at the out-

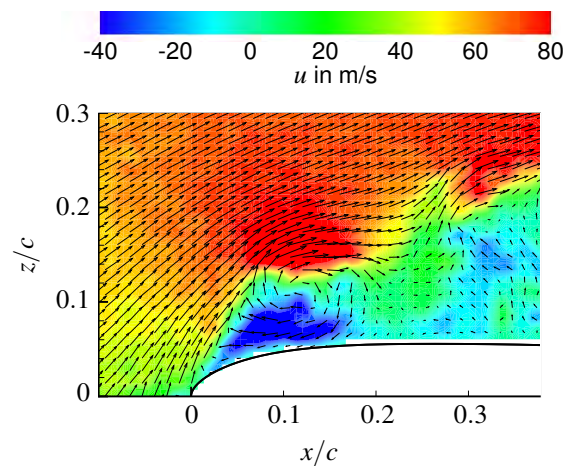


Figure 13: Close-up of  $y/c = 4.07$  in fig. 12, only every second vector in  $x$  and  $z$  is shown.

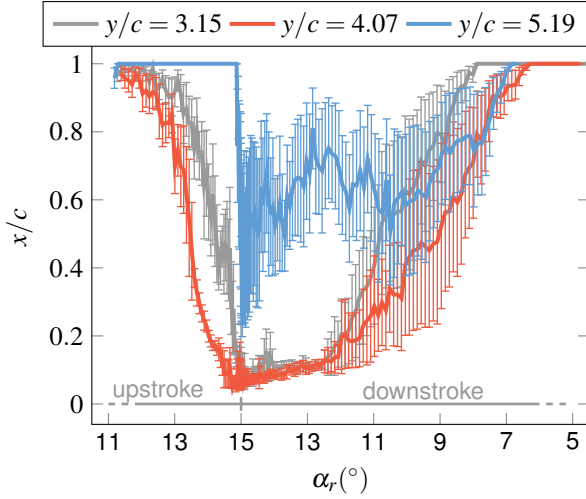


Figure 14: Phase averaged separation points estimated from PIV measurements for a pitching motion of  $\alpha_0 = 9^\circ$ ,  $\alpha_1 = 6^\circ$  and  $k = 0.05$ .

board section. Compared to  $k = 0.025$ , the loads have increased at the two inboard sections but are reduced at the outboard section. A further increase in the reduced frequency to  $k = 0.075$  results in a further reduction of the maximum loads at the outboard section. The maximum lift coefficient increases at the two inboard sections with the stronger increase at  $y/c = 4.07$ . The pitching moment peaks are slightly reduced at  $y/c = 2.96$  and remain nearly constant at  $y/c = 4.07$ . Throughout the limited range of reduced frequencies investigated here, the section  $y/c = 4.07$  shows the strongest peaks in the pitching moment. This can be attributed to a stronger dynamic stall vortex in the area of stall initiation. The influence of the reduced frequency on  $C_{1,\max}$  is small for the outboard section while it is significant for the two inboard sections. The opposite holds true for  $C_{m,\min}$ , where a change in reduced frequency has a stronger impact on the outboard section.

## 4 CONCLUSION

Wind tunnel experiments on a rotor blade tip model with an aspect ratio of 6.2 have been carried out in order to analyze spanwise differences in the static and dynamic stalling characteristics. The measurements were performed at a Reynolds number based on the chord of 900,000 and a free stream Mach number of 0.16. The investigation of static stall was based on data gathered from a quasi-static  $\alpha_r$ -ramp and at static angles of attack. Pitch oscillations with different mean angles of attack including test cases with attached flow, and light and deep dynamic stall were analyzed, as well as influences of the reduced frequency on the sectional aerodynamic loads in deep dynamic stall conditions.

For quasi-static angles of attack the stall onset was found to occur near  $y/c = 4$ , with stall propagating from there in

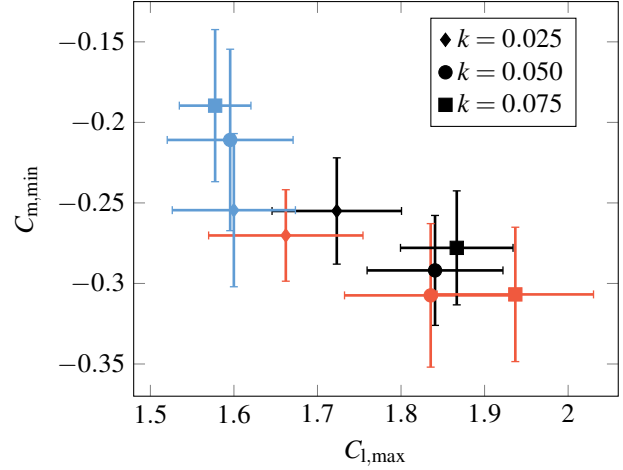


Figure 15: Conditionally averaged maximum lift and negative pitching moment peak at  $y/c = 2.96$  (black),  $y/c = 4.07$  (red) and  $y/c = 5.19$  (blue) for pitching motions of  $\alpha_0 = 9^\circ$  and  $\alpha_1 = 6^\circ$ .

spanwise direction inboard and outboard. Four different stages of flow separation for static angles of attack have been identified:

1. The turbulent boundary layer starts to separate near the trailing edge at  $\alpha_r = 7.2^\circ$ .
2. At the onset of static stall ( $\alpha_r = 11.1^\circ$ ), the turbulent boundary separation moves rapidly upstream to approximately 20% chord. The stalled area has only a limited spanwise extent whereas the flow near the blade tip and the blade root remains attached.
3. With a further increase of  $\alpha_r$ , the static stall spreads further inboard leading to the development of two stall cells.
4. For  $\alpha_r > 14.7^\circ$  the flow separates from the leading edge over most of the span. Near the parabolic blade tip the flow remains partially attached around the leading edge with a significant outboard component of the flow.

The onset of dynamic stall was also found to lie near  $y/c = 4$ . For light dynamic stall, the spanwise spreading of the separation is limited to an area around  $y/c = 4$ . For deep dynamic stall conditions, the dynamic stall development progresses fastest near  $y/c = 4$  and consequentially the leading edge vortex appears first at this section. The influence of the tip vortex is twofold: during times with attached flow, the lift at the outboard section near the parabolic blade tip is reduced and the pressure drag is increased, as expected from inviscid theory. During the dynamic stall, the lift remains higher at the outboard section because the streamwise vorticity accumulating near the wing tip is effectively pinning the dynamic stall vortex down. As a consequence, the peaks in the aerodynamic loads are

smaller at the outboard section as well. For the range of reduced frequencies investigated in this study, the differences in the maximum aerodynamic loads between the section near the parabolic blade tip and the inboard sections increased with reduced frequency.

#### ACKNOWLEDGMENTS

Funding through the DLR project STELAR and the DFG project "Untersuchung der dreidimensionalen dynamischen Strömungsablösung an Rotorblättern" is gratefully acknowledged. Valuable discussions with Tony Gardner and with our colleagues at the ONERA Applied Aerodynamics Department DAAP/H2T in the framework of the EDIRHE-STELAR cooperation are highly appreciated. Furthermore, we would like to thank Moritz Schmidt for his constant support during the design and manufacturing of the wind tunnel model.

#### REFERENCES

- [1] JD Anderson Jr, S Corda, and DM Van Wie. Numerical lifting line theory applied to drooped leading-edge wings below and above stall. *Journal of Aircraft*, 17(12):898–904, 1980.
- [2] WG Bousman. A qualitative examination of dynamic stall from flight test data. *Journal of the American Helicopter Society*, 43(4):279–295, 1998.
- [3] LW Carr. Progress in analysis and prediction of dynamic stall. *Journal of Aircraft*, 25(1):6–17, 1988.
- [4] F Coton and R Galbraith. An examination of dynamic stall on an oscillating rectangular wing. In *21st Applied Aerodynamics Conference*. AIAA 2003-3675, June 2003.
- [5] AD Gardner. User guide for cp2cl plusm v3.x: A program to provide forces and moments from airfoil pressure. Technical Report DLR-IB 224-2014, DLR, 2014.
- [6] AD Gardner and K Richter. Boundary layer transition determination for periodic and static flows using phase-averaged pressure data. *Experiments in Fluids*, 56(6), 2015.
- [7] FB Gustafson and GC Myers Jr. Stalling of helicopter blades. Technical report, NACA, 1946.
- [8] FD Harris and RR Pruyn. Blade stall – half fact, half fiction. *Journal of the American Helicopter Society*, 13(2):27–48, 1968.
- [9] NCG Isaacs and RJ Harrison. Identification of retreating blade stall mechanisms using flight test pressure measurements. In *AHS, 45th Annual Forum*, 1989.
- [10] NL Johnson, S Kotz, and N Balakrishnan. Continuous univariate distributions Vol. 1. In *Wiley series in probability and mathematical statistics : Applied probability and statistics*, pages 156-158. Wiley, 1994.
- [11] K Kaufmann, M Costes, F Richez, AD Gardner, and A Le Pape. Numerical investigation of three-dimensional static and dynamic stall on a finite wing. *Journal of the American Helicopter Society*, 60(3):1–12, 2015.
- [12] A Le Pape, G Pailhas, F David, and JM Deluc. Extensive wind tunnel measurements of dynamic stall phenomenon for the OA209 airfoil including 3D effects. In *Proceedings of the 33rd European Rotorcraft Forum*, pages 320–335, 2007.
- [13] PF Lorber. Tip vortex, stall vortex, and separation observations on pitching three-dimensional wings. In *23rd Fluid Dynamics, Plasmadynamics, and Lasers Conference*, AIAA 93-2972, July 1993.
- [14] PF Lorber, FO Carta, and AF Covino Jr. An oscillating three-dimensional wing experiment: Compressibility, sweep, rate, waveform, and geometry effects on unsteady separation and dynamic stall. Technical report, United Technologies Research Center, East Hartford, CT 06108, 1992.
- [15] WJ McCroskey. Unsteady airfoils. *Annual review of fluid mechanics*, 14(1):285–311, 1982.
- [16] WJ McCroskey, KW McAlister, LW Carr, SL Pucci, O Lambert, and RF Indergrand. Dynamic stall on advanced airfoil sections. *Journal of the American Helicopter Society*, 26(3):40–50, 1981.
- [17] CB Merz, CC Wolf, K Richter, K Kaufmann, and M Raffel. Experimental investigation of dynamic stall on a pitching rotor blade tip. In *STAB Symposium München*, 2014.
- [18] K Mulleners, A Le Pape, B Heine, and M Raffel. The dynamics of static stall. In *16th Int Symp on Applications of Laser Techniques to Fluid Mechanics Lisbon, Portugal, 09-12 July*, 2012.
- [19] K Mulleners and M Raffel. Dynamic stall development. *Experiments in Fluids*, 54(2), 2013.
- [20] JJ Philippe. Définition et évaluation de nouvelles extrémités de pales de rotors d'hélicoptère. Technical report, ONERA-TAP - 92-179, 1992.
- [21] RA Piziali. 2-D and 3-D oscillating wing aerodynamics for a range of angles of attack including stall. NASA Technical Memorandum 4632, NASA, 9 1994.
- [22] M Raffel, CE Willert, ST Wereley, and J Kompenhans. *Particle Image Velocimetry – A Practical Guide*. Springer, 2nd edition, 2007.
- [23] F Scarano. Iterative image deformation methods in PIV. *Measurement Science and Technology*, 13(1):R1–R19, 2002.
- [24] SJ Schreck and HE Helin. Unsteady vortex dynamics and surface pressure topologies on a finite pitching wing. *Journal of Aircraft*, 31(4):899–907, 1994.
- [25] A Spentzos, GN Barakos, KJ Badcock, BE Richards, P Wernert, S Schreck, and M Raffel. Investigation of three-dimensional dynamic stall using computational fluid dynamics. *AIAA Journal*, 43(5):1023–1033, 2005.
- [26] AE Winkelmann and JB Barlow. Flowfield model for a rectangular planform wing beyond stall. *AIAA Journal*, 18(8):1006–1008, 1980.
- [27] H Yeo and M Potsdam. Rotor structural loads analysis using coupled computational fluid dynamics/computational structural dynamics. *Journal of Aircraft*, 2015. published online.